scientific reports

Check for updates

OPEN

Exploring tubulin-paclitaxel binding modes through extensive molecular dynamics simulations

Marine Bozdaganyan[1,2], Vladimir Fedorov[2], Ekaterina Kholina[2], Ilya Kovalenko[2], Nikita Gudimchuk[3]✉ & Philipp Orekhov[1,2,4]✉

Cancer treatment remains a pressing challenge, with paclitaxel playing a pivotal role in chemotherapy by disrupting mitotic spindle dynamics through microtubule stabilization. However, the molecular details of paclitaxel interaction with β-tubulin, its target, remain elusive, impeding efforts to overcome drug resistance and optimize efficacy. Here, we employ extensive molecular dynamics simulations to probe the binding modes of paclitaxel within tubulin protofilaments. Our simulations reveal a spectrum of paclitaxel binding poses, correlated with conformational changes in neighboring residues, proposing the ligand (un)binding route. These diverse binding modes exhibit varied interaction patterns and binding energies, elucidating the complex interplay between paclitaxel-tubulin interactions and the conformational dynamics of the M-loop. Furthermore, key residues influencing paclitaxel affinity and resistance are identified, enhancing our mechanistic understanding of the drug-binding mechanism. Finally, we uncover a novel high-affinity binding mode characterized by paclitaxel penetration into a subpocket formed by helices 1, 7, and loop B9-B10 of β-tubulin concerted with the rotational isomerization around a bond connecting the tetracyclic baccatin core with the N-benzoyl-β-phenylisoserine side chain, offering potential avenues for drug development. Our study advances the understanding of paclitaxel mode of action and informs strategies for rational drug design of antitumor agents.

Keywords Paclitaxel, Taxol, Tubulin, Molecular dynamics simulation, MM/GBSA

Cancer remains one of the most challenging diseases worldwide, necessitating continuous advancements in therapeutic strategies. Among the arsenal of anti-cancer agents, paclitaxel (sold under the brand name Taxol among others) stands as a cornerstone in chemotherapy, exerting its cytotoxic effects by targeting microtubules and blocking division of cancer cells[1]. Paclitaxel binds to β-tubulin near the lateral interface between protofilaments[2–4]. This lateral interface is inherently flexible, as in vitro microtubules can have different numbers of protofilaments, ranging typically from 12 to 15[5,6]. Moreover, tubulin molecules can adopt different conformations, including curved and straight forms, depending on their interactions and the cellular environment[7–10]. Specifically, paclitaxel binding to microtubules inhibits their depolymerization, thereby interfering with normal dynamics of these polymers, critical for search, capture and transport of chromosomes during cell division[11,12]. Although clinically effective, the exact molecular mechanisms of microtubule stabilization by paclitaxel remain unclear. This is primarily due to the dynamic nature of its binding pocket and the limitations of current experimental techniques, which can only provide a static view of the ligand-protein interactions and have yet to achieve atomic resolution.

The outstanding clinical importance of paclitaxel as a cancer chemotherapy agent and a biomedical research tool has kept it in focus in structural and biophysical studies for over three decades. The first reported X-ray structure of the paclitaxel-bound tubulin refined at 3.5 Å resolution, PDB code 1jff[13], was obtained for the zinc-induced tubulin sheets with the non-native lateral contacts and allowed to establish the binding site of paclitaxel at a pocket in β-tubulin that faces the microtubule lumen[2,3] but did not enable the specific conformation of this flexible ligand to be determined with high precision.

In lack of high-resolution model of paclitaxel bound to tubulin, several experimental attempts have been made to identify its bioactive conformation, including the electron density analysis augmented by solution NMR and

[1]Faculty of Biology, Shenzhen MSU-BIT University, Shenzhen 518172, China. [2]Faculty of Biology, Lomonosov Moscow State University, Moscow 119234, Russia. [3]Faculty of Physics, Lomonosov Moscow State University, Moscow 119991, Russia. [4]Sechenov University, Moscow 119146, Russia. ✉email: ngudimch@gmail.com; orekhov_p@smbu.edu.cn

computational methods[14,15], NMR measurements of paclitaxel bound to microtubules[16,17] and in solution[18–22], the synthesis of various conformationally restricted paclitaxel analogs alone[21,23–28] or in combination with molecular modeling[21,29,30]. These efforts ultimately led to the selection of the so-called T-shaped paclitaxel as the most probable β-tubulin-bound conformer[31,32] surpassing other proposed models (e.g., PTX-NY[15], polar[17], and nonpolar[33,34]).

Near-atomic cryoEM structures of paclitaxel bound to microtubules, which appeared later on, brought additionally several important insights[4,35–39]. Firstly, several studies[35–37] indicated a role of paclitaxel in the conformational rearrangement of the M-loop, a flexible structure mediating the stability of lateral contacts between protofilaments (PDB codes 5syf, 5sye, 6wvl, 6wvm, 6wvr, 6ew0). In the work of Debs et al.[40] it was shown that the M-loop acts as a flexible hinge which adopts different angles that disrupt the helical symmetry of microtubules, causing random fluctuations. As a result, perfectly cylindrical microtubules are less stable. At the microtubule seam, the hinge angle can deviate even more, creating a distorted subset of microtubules[37]. However, this distortion disappears when paclitaxel is present that could stabilize microtubules by constraining the β-tubulin M-loop from buckling at the seam. Secondly, the preference of paclitaxel for 'expanded' lattice of the microtubule, suggests it could allosterically affect the extent of longitudinal compaction of the protofilaments[41]. Therefore, there exists a discrepancy in understanding of the molecular mechanism of its action as paclitaxel can affect both longitudinal and lateral contacts within microtubules[11,12,35,38,40–42]. However, the cryoEM structures were obtained with similar to the 1jff structure[13] or even lower resolution of 3.5–5.5 Å and they largely inherited the paclitaxel pose from this earlier X-ray structure, which was used to build the initial models of the microtubule lattice[4].

Recently, Prota et al.[43] have combined crystallographic analysis with molecular dynamics simulations and reported high-resolution X-ray structures of tubulin, liganded with baccatin III, the core moiety of paclitaxel, as well as with engineered paclitaxel analogues. First, it was shown that taxanes bind more effectively to microtubules than to unassembled tubulin as the microtubule assembly is linked to M-loop conformational changes that facilitate access to the taxane binding site, especially for the bulky C13 side chain of taxanes. Second, the authors demonstrated that occupancy of the taxane site does not affect the straightness of tubulin protofilaments. Finally, longitudinal expansion of microtubule lattices occurs even upon binding of the biochemically inactive baccatin III, representing the taxane core, suggesting that this process is unrelated to microtubule stabilization. Thus, this study has helped to clarify some of the key aspects of the binding of taxanes to tubulin and microtubules. However, a high-resolution structure of the complex between paclitaxel and soluble tubulin is still not available, perhaps due to the relatively low affinity of this complex with estimated binding energy of ~ -3.0 kcal/mol[44–48].

In the absence of the high resolution and dynamic information about paclitaxel-tubulin interactions, molecular dynamics (MD) simulations remain an invaluable tool for exploring paclitaxel's interactions with tubulin offering an unprecedented temporal and spatial resolution. Using this approach, not only the lower-resolution structural data can be refined based on physical principles, but also the hidden but essential details of interplay between the drug and protein can be elicited and analyzed. Importantly, MD simulations allow building on and integrating different sources of experimental information, such as X-ray, cryoEM, and NMR.

Several earlier computational studies attempted to explore dynamics of the paclitaxel-tubulin complexes and energetic contributions of individual residues to the binding energy[43,49–57]. Some of these computational studies[43,51,54,56,] were focused on determination of the key amino acids within the paclitaxel binding site by means of MM/PBSA or similar approaches highlighting the role of β-tubulin residues Glu22, Glu27, Arg278, Asp26, Asp226, His229, Arg369, Lys218, Ser277 and Thr276 (according to the residue numeration of 1jff). Molecular dynamics simulations conducted in[50,52,53] examined the role of mutations in the M-loop region and demonstrated that the M-loop is strongly bound to paclitaxel in wild-type tubulin, which restricts its flexibility and is a key factor in microtubule stabilization. Similar results were obtained by Mitra and Sept[49] showed that paclitaxel plausibly stabilizes adjacent protofilament interactions by modulating M-loop dynamics and its contacts with the H1-S2 loop of neighboring β-tubulin. Basu et al.[53] further revealed that paclitaxel increases the correlation between lateral contact regions, and causes the M-loop to lose its secondary structure, shifting from a 310 or α-helix upon binding. However, all of these simulations were restricted to significantly shorter simulation times, not exceeding hundreds of nanoseconds, in contrast to the current study with the total effective length of trajectories surpassing 20 μs.

In this work, we present the results of extensive MD simulations based on three microtubule-paclitaxel structures from the *Sus scrofa*, 3j6g[4], 5syf[35], and 6ew0[37], aimed at elucidating the binding modes of paclitaxel within its binding pocket in tetrameric tubulin protofilaments. We focused on the three major points: (1) investigating the dynamic binding modes of paclitaxel to microtubules; (2) exploring local and global conformational changes in tubulin bound to paclitaxel; (3) analyzing the energetics and contributions of key amino acids to different paclitaxel binding poses. Our simulations elucidate the mechanisms underlying microtubule stabilization by paclitaxel binding at the taxane site on an atomic level, revealing previously unreported ligand conformations with both low and high affinities. These results offer insights into potential avenues for enhancing paclitaxel efficacy through rational drug design efforts and shed light on the ligand binding pathway.

Results

In the present study, we have conducted a series of extensive molecular dynamics simulations of short tetrameric protofilaments with paclitaxel bound to β-tubulins (Fig. 1A). The absence of lateral interfaces with neighboring protofilaments, which were not included in our simulations, imposed considerable limitations on our models, as paclitaxel is believed to affect these lateral contacts, as mentioned in the Introduction. However, we had to omit these details to set up systems of manageable size that would allow for longer simulation time and extensive sampling exceeding any previous simulations reported to date. The initial models for the simulations were constructed based on three available experimental cryoEM structures of microtubules from a single species

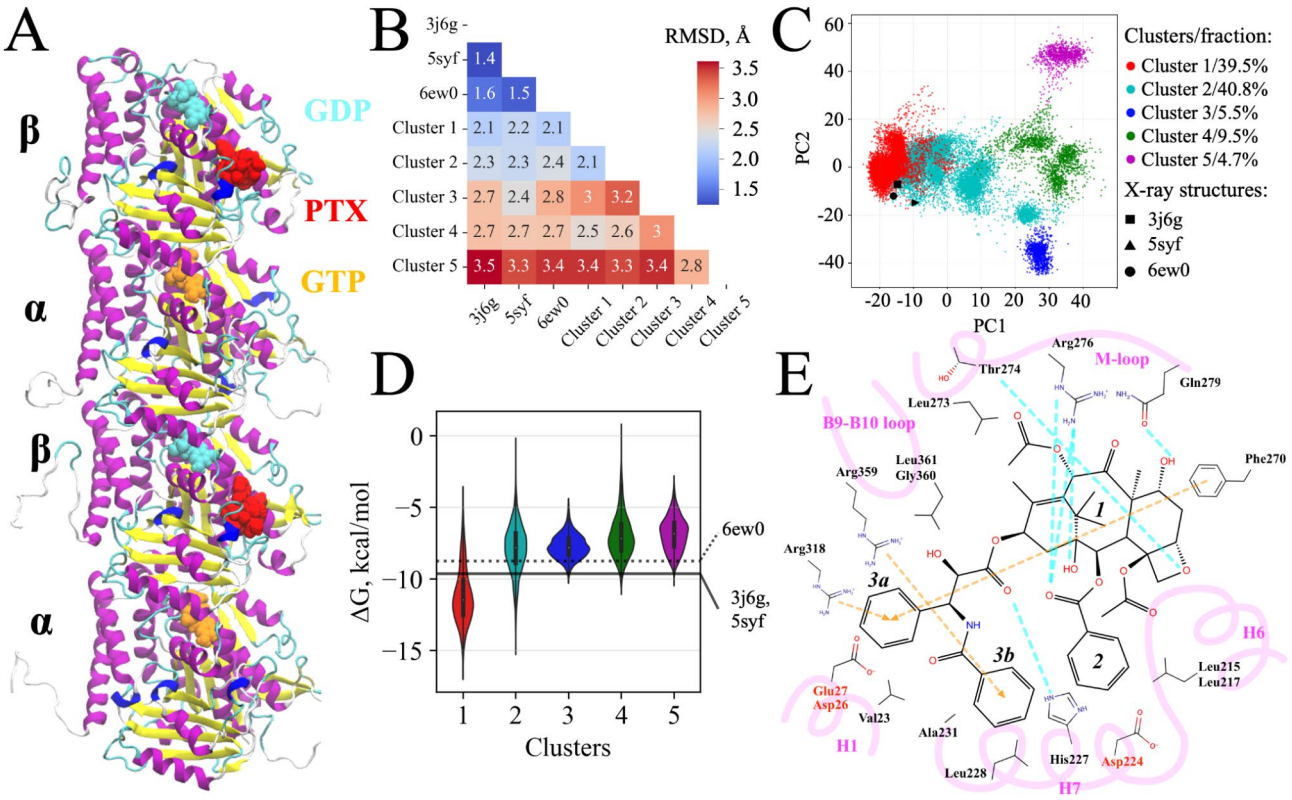

Fig. 1. Cluster analysis of paclitaxel binding poses and binding energy estimation. (**A**) Starting conformation of a tetrameric tubulin protofilament with paclitaxel (PTX) bound to β-tubulin monomers based on the 3j6g experimental structure; (**B**) Root mean square deviations (RMSD) of the heavy atoms belonging to the binding pocket/paclitaxel calculated between three experimental structures and the representative structures of clusters 1–5 with the minimal binding free energy. Refer to Supplementary Tables S1-S2 for the standard deviations and the respective values for paclitaxel alone; (**C**) Projection of conformations of the paclitaxel binding pocket observed in all molecular dynamics simulations onto the two top principal components. Each dot represents a single conformation of paclitaxel with its local amino acid environment. Different colors stand for five identified clusters of conformations. Corresponding global motions are visualized in Supplementary Movies 1 and 2; (**D**) Distributions of paclitaxel binding free energy in each of the determined clusters estimated by means of MM/GBSA. Horizontal lines show the binding energies estimated for the initial experimental structures; (**E**) Scheme illustrating the key residues in the paclitaxel binding site interacting with the ligand. Feasible H-bonds are shown by the cyan dotted lines; the - and cation- interactions - by the yellow arrows. Residue numbers are given according to the standard Uniprot sequence of β-tubulin (Uniprot ID: P02554). The structural moieties of paclitaxel are labeled with numbers: *1*, tetracyclic baccatin core; *2*, benzoyloxy side chain; *3*, N-benzoyl-β-phenylisoserine side chain (*3a*, N-benzoyl; *3b*, β-phenylisoserine).

Sus scrofa in complex with paclitaxel (resolution from 3.50 to 5.50 Å): 3j6g[4], 5syf[35], and 6ew0[37]. We opted to use all three experimental structures as the initial models for simulations with the expectation that the diversity in starting conformations would eventually enhance sampling. For each system, we performed three independent replicate simulations, each lasting at least 1 μs, resulting in a cumulative simulation time exceeding 9 μs. Given that each model protofilament comprises two β-tubulin monomers analyzed separately, the total simulated time was effectively doubled, reaching 19.1 μs.

Molecular Dynamics Simulations Uncover Diverse Binding Poses of Paclitaxel.

Although the initial experimental structures exhibited relatively similar binding poses (RMSD of paclitaxel with its neighboring residues between all of them does not exceed 1.9 Å as shown in Fig. 1B, Tables S1-S2), the MD trajectories revealed a remarkably diverse spectrum of binding poses adopted by the ligand and the neighboring residues of the pocket during the course of simulations. These poses included conformations that closely resembled experimental structures and highly divergent ones, both in terms of paclitaxel orientations in the binding site and conformations of the loops lining the binding pocket. Overall, the tetracyclic baccatin core of paclitaxel is the most rigid part of the ligand roughly corresponding to the most prominent region of the experimental densities (Figure S1) while all of its substituents appear highly mobile throughout the simulations. Meanwhile, the M-loop region of β-tubulin is the most flexible part of the protein in the vicinity of paclitaxel (refer to Figure S2 for corresponding root mean square fluctuations, RMSF).

In order to systematize the observed diversity of binding poses we applied agglomerative clustering to the top principal components obtained for the aligned atomic positions of paclitaxel and the nearby amino acids

in the paclitaxel binding site. The first two principal components are dominated by the paclitaxel motion and correspond to the displacement of its N-benzoyl-β-phenylisoserine side chain from the subpocket lined by the C-terminus of H7 helix and B9-B10 loop (principal component 1, Supplementary Movie 1) and rearrangement of its tetracyclic baccatin core together with the benzoyloxy side chain accompanied by the M-loop motion and reshaping (principal component 2, Supplementary Movie 2). The analysis identified five distinct clusters of conformations (see Fig. 1C). Although the overall RMSD distances (averaged across all atoms of paclitaxel and and the residues in the binding site) between the clusters do not exceed 3.5 Å (Fig. 1B, see Supplementary Table S1 for standard deviations), the RMSD for paclitaxel alone reaches 8.9 Å (Supplementary Table S2), reflecting the dominance of ligand mobility over the binding site reshaping in the top principal components. We were further able to estimate the mean binding energy of paclitaxel in each cluster (Fig. 1D, Table S3) as well as to identify the lowest energy conformations in each cluster by employing the MM/GBSA method. The obtained clusters were assigned numbers from 1 to 5 according to their mean energies starting from the minimal one. The pairwise independent t-test confirmed the statistical significance of the differences in the binding energies across all clusters (p-values < 0.002, Supplementary Table S4).

Two clusters with the lowest mean energy, 1 and 2, dominate in the simulated ensemble, collectively encompassing over 80% of all conformations. Both of these dominant clusters remain relatively similar to the paclitaxel poses in the experimentally determined structures with cluster 2 comprising the initial experimental conformations (see Fig. 1C, Tables S1-2). During the simulations, we observed multiple transitions between clusters 1 and 2, which occurred in both directions with almost equal frequencies suggesting that the two states remain in the detailed equilibrium (Fig. 2A). Nonetheless, cluster 1 has several distinct peculiarities detailed in the corresponding section below, which apparently result in a sufficiently lower estimation for the paclitaxel binding energy. Its mean value is lower than the binding energy averaged over the three experimental structures by approximately 1.9 kcal/mol ($\Delta G^{cluster\ 1}_{bind,\ mean}$ = -11.16 kcal/mol, $\Delta G^{exp}_{bind,\ mean}$ = -9.3 kcal/mol). However, this energetic gain might be counteracted by reduced mobility of paclitaxel in cluster 1 as compared to cluster 2 (see Figure S2 B-C).

The other identified clusters 3–5 are more divergent from the starting conformations and have significantly higher mean binding energies, ranging from $\Delta G^{cluster\ 3}_{bind,\ mean}$ = -7.72 kcal/mol to $\Delta G^{cluster\ 5}_{bind,\ mean}$ = -6.86 kcal/mol. Strikingly, the binding energy of individual conformations in cluster 4 can even reach positive values suggesting that these conformations might correspond to feasible binding/unbinding intermediates. These clusters can be accessed from cluster 2, while clusters 3 and 5 can be only reached from clusters 2 and 4, respectively. All the transitions between connected clusters appear reversible (Fig. 2A, Supplementary Figures S3-S5). Importantly, the transition to cluster 3 is accompanied by a complete unfolding of the otherwise partially (in clusters 1–2) or even almost completely α-helical (in clusters 4–5) M-loop (see Fig. 2B-F). This drastic conformational rearrangement of the M-loop allows for the formation of a favorable H-bond between paclitaxel (oxygen atom 1OI4) and the backbone amino group of Gly 277 (see Fig. 2D, Supplementary Table S5, and Figure S6). However, in clusters 4–5, this glycine residue is involved in an alternative H-bond with Tyr 281 stabilizing the α-helical conformation of the M-loop (Fig. 2E-F). The observed folding and reorientation of the M-loop disrupts several favorable interactions between the unstructured/less structured M-loop and paclitaxel, which are present in clusters 1–3. This includes the breakage of the hydrogen bonds with Gln 279 and Arg 276 (Supplementary Figure S6), thus creating an opportunity for the ligand to unbind. This observation aligns with the binding energy estimates provided earlier and correlates with the increase in distance between the ligand and the geometric center of the binding site: from below 5 Å in cluster 1 to around 10 Å in cluster 5 (Supplementary Figure S7).

It is important to note that while the starting conformations of paclitaxel and surrounding residues in all three experimental structures are only slightly different (as indicated by the RMSD values shown in Fig. 1B and Tables S1-S2 and reflected in the relatively small difference in the binding energies, which is ~0.9 kcal/mol for 3j6g/6ew0 and 5syf/6ew0, and almost negligible for 3j6g/5syf, see Table S3), the explored conformational space depended to a certain degree on the starting conformation (see Figure S8). While the systems thoroughly explored the regions of the conformational space corresponding to clusters 1 and 2 regardless of the initial conformation, cluster 4 is mainly explored in the simulations started from 6ew0 and only transiently visited in the simulations started from 3j6g, while cluster 3 and cluster 5 are visited solely in the simulations started from 5syf and 6ew0, respectively. While this can be partially explained by the inevitably limited sampling of such a complex system as a paclitaxel-bound protofilament, it might be also attributed to a slight unavoidable difference in the starting conformations (e.g., the central structure of cluster 3 has slightly lower RMSD to 5syf as compared to 3j6g/6ew0, see Supplementary Tables 1–2).

Also, given that the unrestrained free protofilaments rapidly adopt a curved conformation both in the present molecular dynamics simulations (Figure S9), we have additionally explored the potential impact of the overall protofilament shape on the dynamics of paclitaxel within the binding pocket. For this purpose, a supplementary set of simulations was run for the 5syf tetramer, wherein positional restraints were applied to the distal protein regions relative to the paclitaxel site such that the "straight" conformation of protofilaments as present in the initial model of a microtubule were preserved throughout entire simulations without affecting directly the mobility of paclitaxel and the protein residues in its vicinity. The resulting trajectories exhibited that paclitaxel in the "straight" protofilament undergoes translocation resembling the one corresponding to the first principal component of the "curved" trajectories, specifically, the displacement of its N-benzoyl-β-phenylisoserine side chain from the subpocket formed by the C-terminus of H7 helix and B9-B10 loop. However, we did not observe its further motion and rearrangement of the M-loop along the second PC (Figures S10). This finding suggests that protofilament bending/straightening does not affect the initial paclitaxel binding mode at least at the explored timescale of several microseconds but it can impede the M-loop reshaping presumably required for ligand unbinding.

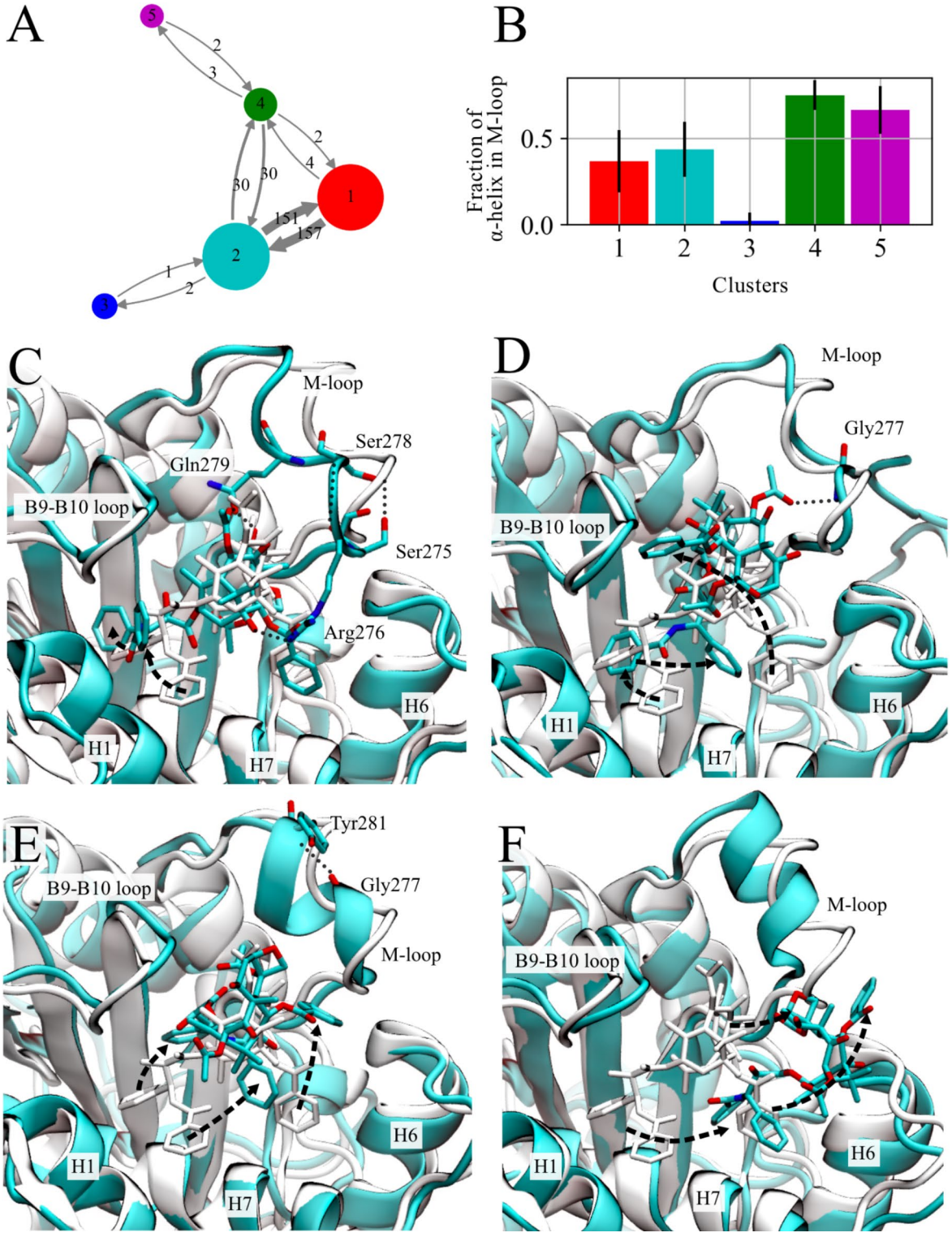

Fig. 2. Flexibility of paclitaxel and plasticity of M-loop. (**A**) a scheme showing the number of observed transitions between the identified clusters of conformations (sizes of circles correspond to the populations of the corresponding clusters, their colors match those in Fig. 1); (**B**) Fraction of α-helical content in the M-loop (residues 274–285) in the identified clusters of the paclitaxel/binding pocket conformations, error bars correspond to the standard deviations; (**C**–**F**) Conformations of paclitaxel in its binding site with the lowest ΔG_{bind} from clusters 1, 3, 4, and 5, respectively, (paclitaxel is shown using the element wise-colored sticks, protein is represented as the cyan cartoon) superimposed with the experimental structure 6ew0 (white sticks and cartoon). The black arrows indicate the motions of large paclitaxel moieties with respect to the experimental structure; dotted lines show key H-bonds.

Contributions of individual amino acids to the binding energy

Decomposition of the MM/GBSA binding energy into contributions from individual amino acids allowed us to reveal key stabilizing and destabilizing interactions between paclitaxel and β-tubulin within each cluster in detail (see Fig. 1E for the scheme illustrating the key interacting residues and Fig. 3 for their energetic contributions in each cluster). As such key interactions we have chosen the residues with the contribution to the total binding energy exceeding 0.5 kcal/mol by the absolute value (the full list is provided in Table S6). The number of these residues decreases as we move from cluster 1 (20 residues) to cluster 5 (8 residues), a trend which agrees with the increasing average binding free energy in this sequence. Among such residues, only two appear in common between all 5 clusters: His 227 and Leu 215 (see Table S7). The former residue belongs to H7 and it is capable of forming H-bonds with paclitaxel (see Table S5, Figure S6 for the H-bond population analysis), while the later belongs to a large group of hydrophobic residues at the C-terminus of helix H6, which interacts with the benzoate and tetracyclic moieties of paclitaxel. A number of other residues contribute to this hydrophobic cluster including Leu 217, Leu 228, Leu 273, Gly 360, Ala 231, and Leu 361. The latter two residues appear as the key residues in all clusters apart from cluster 5. A few other residues, which are stabilizing paclitaxel in the binding site and worth noting, include Arg 318 (only in cluster 1) and Phe 270 (clusters 1, 3), which participate in π-cation and π-π stacking interactions with paclitaxel, respectively, Thr 274 (H-bond donor via the backbone amino group, only in cluster 1), and Gln 279 (H-bond acceptor, clusters 1, 2, and 4).

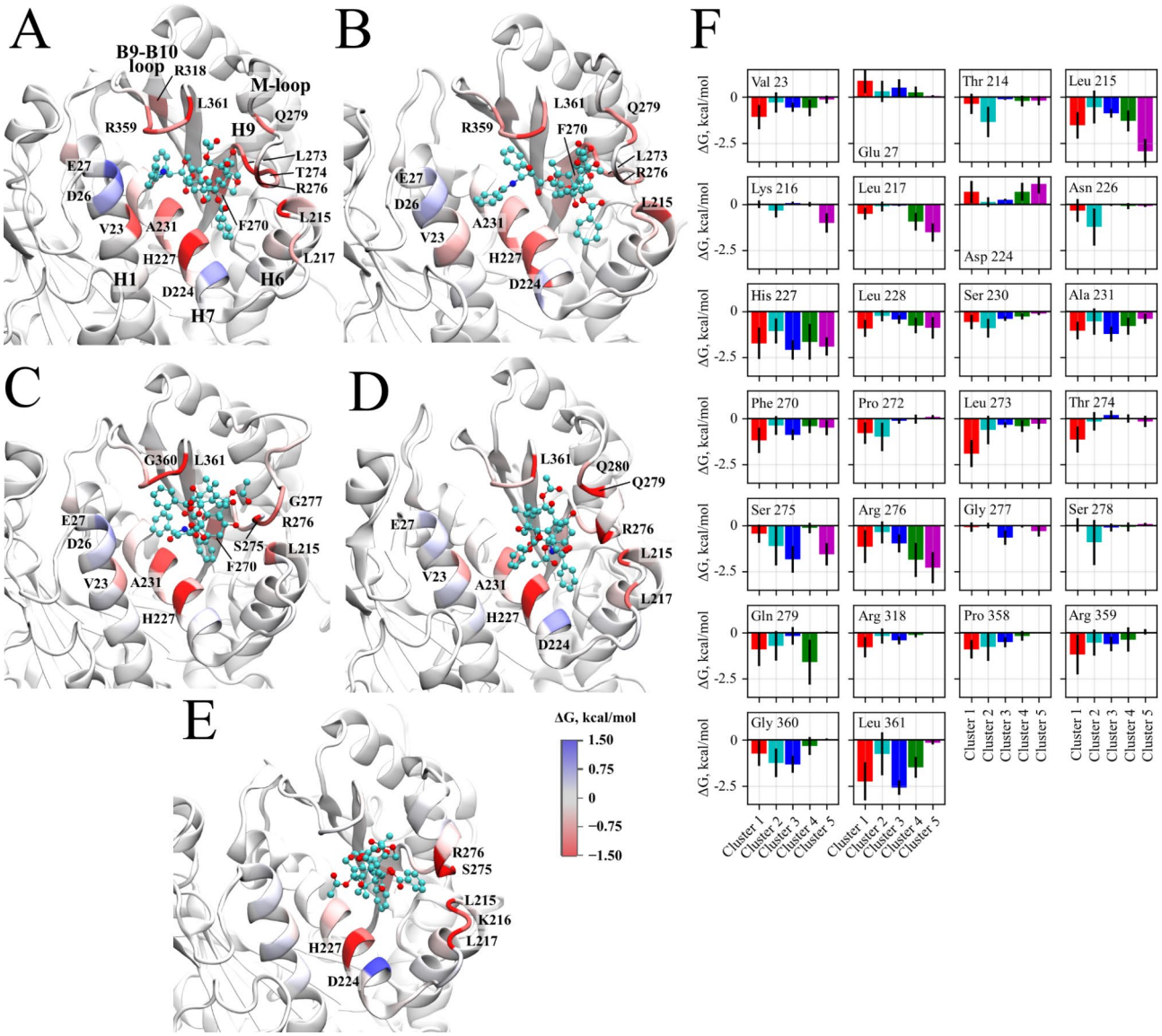

Fig. 3. Energy contributions of individual residues to the binding energy. (**A**–**E**) Conformations of the paclitaxel binding site with the lowest ΔG_{bind} from each cluster from cluster 1 to cluster 5. Residues are colored according to their contribution to the binding free energy. Key residues and protein regions are captioned; **F**: Contributions of individual residues in the binding pocket to the total binding free energy in each cluster of conformations. Colors match those in Fig. 1.

As previously mentioned, conformations observed in clusters 4–5, characterized by the lowest estimated affinities, likely represent intermediate states in the binding/unbinding process. This is evidenced by significant changes in the interaction pattern between paclitaxel and the residues of the binding pocket. Specifically, while interactions with residues in the B9-B10 loop and the C-terminal region of H7 diminish, contributions from residues in the H6-H7 loop increase, coinciding with translocation of paclitaxel into a subpocket bordered by the N-termini of the M-loop and H7 in addition to the H6-H7 loop.

Two key destabilizing residues (i.e., with the positive contribution to the binding energy) are negatively charged Glu 27 and Asp 224. Both residues are situated near the benzene rings of paclitaxel perturbing otherwise largely hydrophobic subpockets. Meanwhile, the destabilizing contributions of these residues are compensated by neighboring positively charged residues Arg 318/359 and His 227, respectively. Glu 22 and Asp 26 and two additional destabilizing residues, however, both of them have much smaller contributions to the total binding free energy. Apparently, the presence of negatively charged residues in the paclitaxel pocket weakens its affinity to β-tubulin due to their repulsion from the proximal aromatic rings of paclitaxel.

Peculiarities of the high affinity binding pose

The primary structural feature of cluster 1 (characterized by the lowest binding energy among all explored structures, $\Delta G^{cluster\ 1}_{bind,\ min}$ = -16.36 kcal/mol, see Table S3) is the enhanced capability of paclitaxel to explore a subpocket of the binding site formed by helices H1, H7, and loop B9-B10 (see Figs. 2C and 3A). The opening of this subpocket results in decrease of the paclitaxel-binding site distance in cluster 1 as compared to cluster 2 (see Figure S7). It is noteworthy that this distance displays strong correlation with the paclitaxel binding energy across all five identified clusters.

We have further identified the residues contributing to the lower ($\Delta\Delta G_{cluster\ 1-exp}$= -1.9 kcal/mol) binding energy of paclitaxel in cluster 1 in comparison to the initial experimental structures (Fig. 4A-B) based

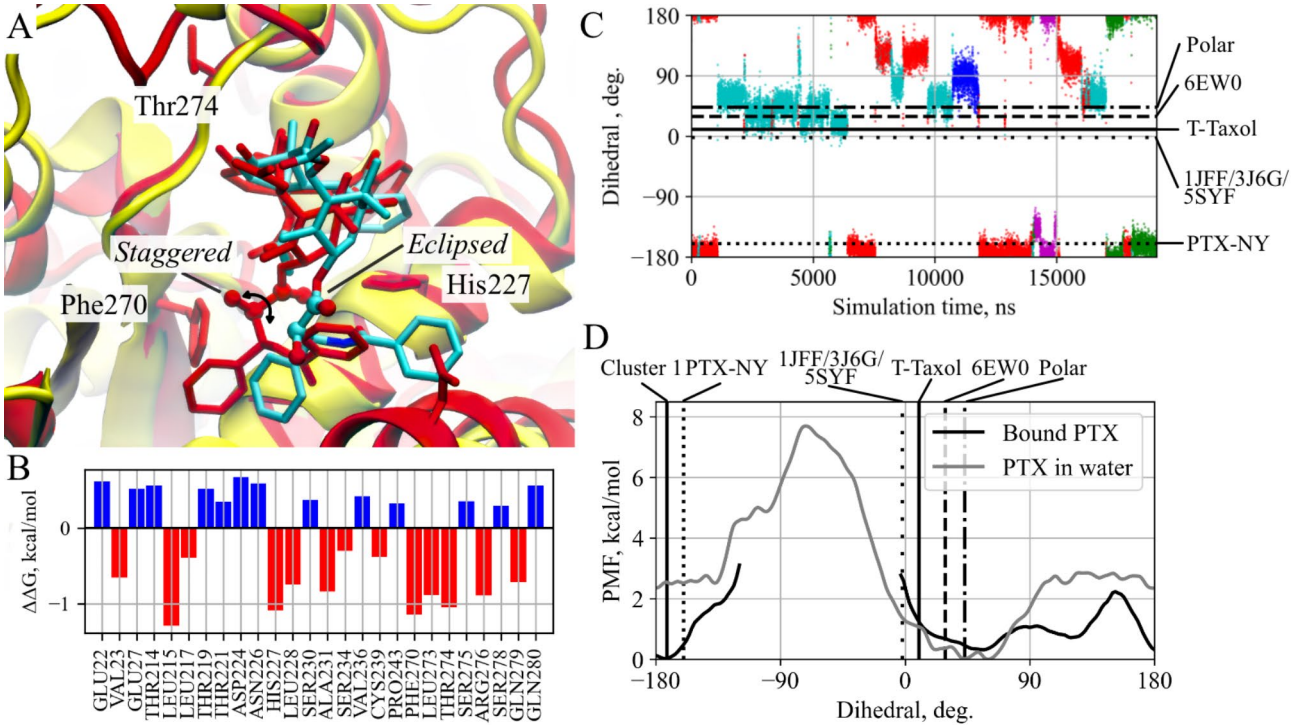

Fig. 4. Paclitaxel conformations with the lowest ΔG_{bind} from molecular dynamics simulations, experimental structures, earlier models, and in solution. (**A**) Structure with the lowest ΔG_{bind} from molecular dynamics simulations (cluster 1, red cartoon and sticks) aligned to the experimental structure 3j6g (yellow cartoon and colored sticks). Key residues affecting the binding free energy are shown in red. The black arrow points to the OBB1-CBB-CB1-OB1 dihedral in the N-benzoyl-β-phenylisoserine side chain, which undergoes the *eclipsed/staggered* isomerisation; (**B**) Contributions of individual amino acids to the $\Delta\Delta G_{bind}$ between the lowest ΔG_{bind} conformation from MD and experimental structures (averaged over 3j6g, 5syf, and 6ew0). Negative values correspond to more favorable interactions in the MD conformation compared to the experimental structures; (**C**) Evolution of the OBB1-CBB-CB1-OB1 dihedral throughout the simulations. Colors indicate the clusters of conformations; vertical lines correspond to the values observed in the experimental structures and in several earlier proposed structural models of paclitaxel[31]; (**D**) Potential of mean force estimated for the OBB1-CBB-CB1-OB1 dihedral. The black line shows the profile for paclitaxel bound to tubulin obtained from the performed simulations of protofilaments. The gray line shows the profile for free paclitaxel in water estimated using umbrella sampling. Vertical lines indicate the dihedral value observed in the lowest ΔG_{bind} structure (cluster 1), in the experimental structures and in the previously proposed models.

on the residue-wise decomposition of the MM/GBSA energies. They include Phe 270, which is involved into the favorable π-π interaction with the N-benzoyl ring of paclitaxel, several hydrophobic residues (Leu 215, Leu 273), as well as Arg 276, His 227, and Thr 274 forming hydrogen bonds with paclitaxel.

The observed penetration of paclitaxel into this subpocket is accompanied by an *eclipsed/staggered* isomerisation around a bond connecting the tetracyclic baccain core to the N-benzoyl-β-phenylisoserine side chain of the compound (Fig. 4A), which adopts the values around −170° (*staggered*) in cluster 1 against approx. 0°-30° (*eclipsed*) in cluster 2 and the experimental structures (see Fig. 4C). Notably, the *staggered* conformation aligns with the previously proposed PTX-NY model[15], while the *eclipsed* conformation is observed in two alternative paclitaxel models: the polar model[17] and T-taxol[14] (the values are shown in Fig. 4C). The interconversion between the *staggered* and *eclipsed* conformations observed in the simulations provides a potential explanation for the apparent contradiction between the PTX-NY and T-taxol models, which has been extensively debated in the literature[31,32].

To further explore the conformational plasticity of paclitaxel around this bond, we have estimated the free energy profiles for the rotation around this bond in protein and in water using the Boltzmann inversion of the dihedral distribution in the MD trajectories for the tubulin-bound paclitaxel and the umbrella sampling approach for a single paclitaxel molecule in water. The resulting profiles (Fig. 4D) indicate that this dihedral has a single free energy minimum in case of paclitaxel in aqueous solution, which corresponds to the *eclipsed*-conformation similar to those observed in the experimental structures. The free energy of the *staggered*-conformation in water appears approx. 2.5 kcal/mol higher. However, the protein environment renders this *staggered*-conformation equally favorable with the free energy profile featuring two alternative minima in this case. The two conformations are separated by a relatively low free energy barrier of approx. 2 kcal/mol, which allows for transitions between the two isomers observed throughout the simulations. Importantly, such *staggered*-conformations were also observed in the simulations of restrained "straight" protofilaments indicating that the isomerisation is not related to the protofilament curving observed in our simulations (Figure S11).

Discussion

Our study sheds light on the binding modes of paclitaxel within its binding pocket in tetrameric tubulin protofilaments employing extensive atomistic molecular dynamics simulations exceeding 20 μs of the effective simulation time. The simulations unveil that paclitaxel does not maintain a static position in the binding pocket; instead, it adopts a plethora of binding poses associated with the conformational rearrangement of neighboring residues. The clustering analysis identifies five distinct clusters of conformations, with clusters 1 and 2 dominating the simulated ensemble. These clusters feature binding energies that are either similar to or lower than the binding energies estimated for the initial experimental atomistic models (mean binding energies for clusters 1 and 2 equal −11.16 and −7.89 kcal/mol, respectively). These values are close to the experimental value of paclitaxel binding affinity to microtubules (estimated at -10.8 kcal/mol[58]) and significantly higher than its affinity to free tubulin (~ -3 kcal/mol[44–48]). On the other hand, clusters 3–5 are less populated and possess higher mean binding energies. All of the identified clusters exhibit distinct interaction patterns between paclitaxel and the binding pocket residues with the total number of strongly interacting residues and the distance between paclitaxel and the center of the binding pocket correlated to their MM/GBSA binding energies suggesting that the low-affinity conformations might correspond to intermediates of the paclitaxel (un)binding route. Such conformations maintained by stronger interactions of paclitaxel with residues belonging to the N-termini of the M-loop and H7 (i.e., K216, L217, S275) were not reported in earlier simulation studies[43,51,56] (Supplementary Table 8) apparently due to less sufficient sampling.

Our simulations of paclitaxel-bound tetrameric protofilaments did not reveal any notable differences from previous simulations of GTP- and GDP-protofilaments without paclitaxel[10,59–62] in terms of the shape of protofilaments. Regardless of the paclitaxel presence, the free protofilaments adopted a curved conformation (see Figure S9). Furthermore, supplementary simulations conducted here on paclitaxel-bound protofilaments in the "straight" conformation, maintained by the positional restraints, which did not interfere with the paclitaxel pocket, indicated that regardless of the protofilament's straightness, the taxane pocket did not undergo significant reshaping, and the conformational space explored by paclitaxel remained largely unaffected. This observation aligns well with recently reported simulations by Prota et al.[43], which also emphasized that the occupancy of the taxane site does not influence the straightness of tubulin protofilaments.

Mobility of paclitaxel

While the tetracyclic baccatin core of paclitaxel remains relatively rigid, its substituents display considerable mobility throughout the simulations. These observations are in line with the relatively low densities observed for both benzoyloxy and N-benzoyl-β-phenylisoserine side chain in the 1jff X-ray structure[13], which are also poorly resolved in the available cryoEM structures of the microtubules stabilized by paclitaxel (3j6g, 5syf, and 6ew0, see Figure S4) indicating their highly dynamic nature, which cannot be adequately described by a single static conformation. Indeed, in our simulations these substituents undergo significant rearrangements as illustrated in Fig. 2C-F. While in cluster 1, the N-benzoyl-β-phenylisoserine chain penetrates deeper into the subpocket formed by the B9-B10 loop and the C-terminus of helix H7 resulting in a tighter binding of paclitaxel as indicated by lower values of the MM/GBSA binding energy estimates, in cluster 3 the two aromatic rings (N-benzoyl and 3'-phenyl) of the N-benzoyl-β-phenylisoserine moiety swap concurrently with the benzoyloxy group relocation from its subpocket near helices H6/H7 into the opposite part of the binding pocket bordered by loop B9-B10. Finally, in cluster 5 the N-benzoyl-β-phenylisoserine chain replaces the benzoyloxy substituent in its subpocket, while the later completely leaves the paclitaxel site. Apparently, this gradual "jumping" of aromatic rings stabilizes the (un)binding intermediates and suggests the following scenario for the paclitaxel binding: (1) the N-benzoyl-β-phenylisoserine chain binds to the H6/H7 subpocket; (2) it moves toward the B9-B10 loop/H1/

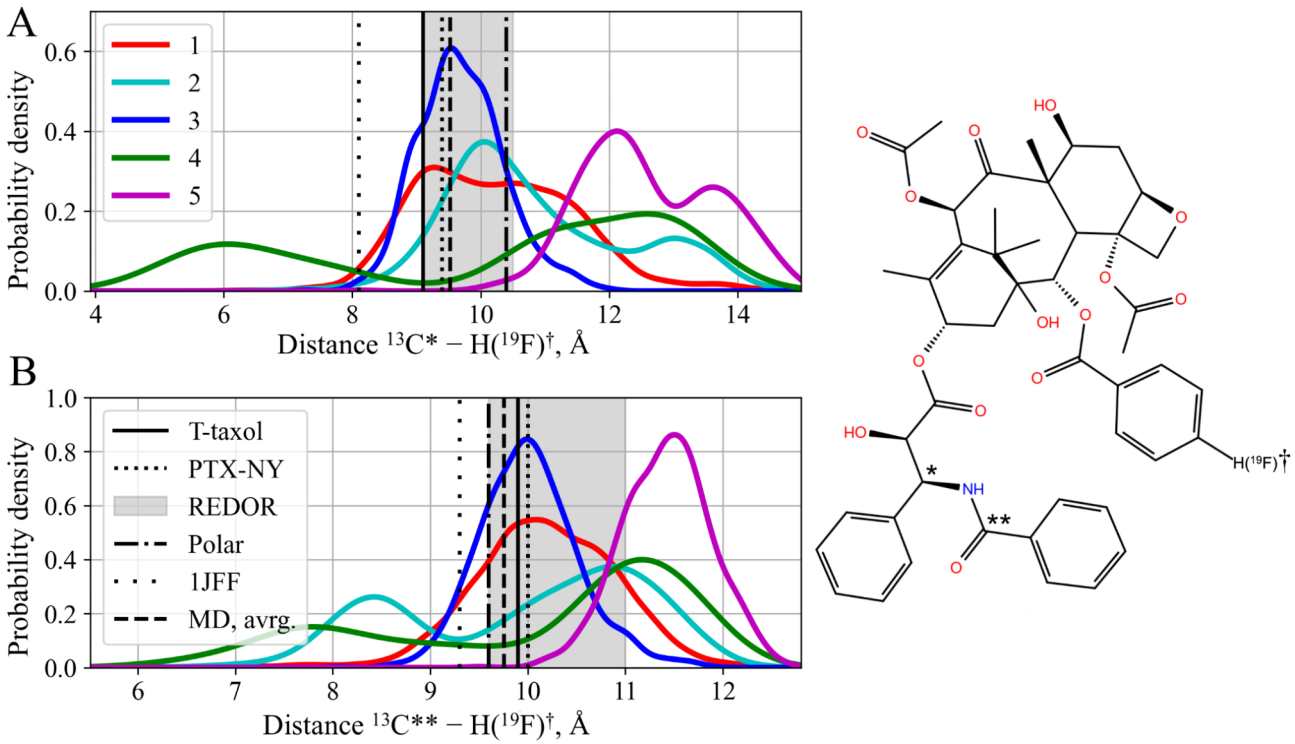

Fig. 5. Comparison of intramolecular distances in microtubule-bound paclitaxel from MD simulations, REDOR measurements, and several previously proposed structural models. (**A**,**B**) Distributions of two C-H(F) distances in the five observed clusters of MD trajectories, the respective values from previously reported structural models of paclitaxel, and their experimental REDOR estimates measured for a fluorinated paclitaxel analog shown in right (gray area indicates the error margins).

H7 subpocket, (3) allowing the benzoyloxy group to replace it. These observations support an earlier hypothesis that the H6/H7 loop may serve as an initial low-affinity paclitaxel binding site en route to the high-affinity site[58].

Comparison of the simulated conformations with NMR data

Earlier solid state ^{13}C-^{19}F REDOR NMR experiments with the fluorinated paclitaxel derivative bound to microtubules by Li et al.[17] allowed to measure two ^{13}C-^{19}F intramolecular distances between the benzoyloxy and the N-benzoyl-β-phenylisoserine side chains of this fluorinated taxoid. Several structural models of the microtubule-bound paclitaxel have been proposed based on these two REDOR distances (involving two carbon atoms and a fluorine atom at the para-position of the benzoyloxy group, labeled as */** and † in Fig. 5, respectively) and low resolution electron diffraction data assisted by computational modeling, including polar[17], T-taxol, and PTX-NY[15] models. We compared the REDOR estimates for these distances with their distributions in the present molecular dynamics simulations. The distances averaged over the simulations fall within the error margins of the REDOR measurements (see Fig. 5A-B). Most of the previously proposed structural models[31] are also consistent with these distances, except for the conformation present in the X-ray structure 3jff. Furthermore, the distance distributions for different clusters in the simulations align more closely with the distances in specific models: T-taxol corresponds to cluster 1, while PTX-NY resembles the conformations in cluster 3.

Overall, the dynamic ensemble of paclitaxel poses observed in the simulations aligns with the REDOR data and includes conformations with intramolecular distances corresponding to all previously proposed static structural models of the bioactive paclitaxel structure. The broad distributions of these distances and the OBB1-CBB-CB1-OB1 dihedral, which undergoes the *staggered*/*eclipsed* transitions (Fig. 4), encompass all earlier models and support the idea that the conformational ensemble of paclitaxel cannot be adequately captured by a single static structure. Therefore, this finding helps to resolve apparent contradictions between different static models.

Diversity of the M-loop conformations

Apart from the paclitaxel side chains, the M-loop of β-tubulin also exhibits notable flexibility in agreement with the low experimental electron/EM densities corresponding to this region as well. The M-loop in the prototypical X-ray structure of tubulin in complex with paclitaxel (PDB code 1jff) coordinates the zinc ion and as a result it appears in a completely different conformation from what was observed in the context of the microtubule lattice using the cryoEM technique[35]. Recent high-resolution crystallographic structures of tubulin in complex with several analogs of paclitaxel[43] provided additional details about ligand binding in the paclitaxel site, but they also failed to resolve part of the M-loop and detect large structural rearrangements between apo- and taxane-bound

tubulin structures suggesting that the ligand effects could be associated with the dynamic behavior of β-tubulin and its M-loop, particularly.

Our simulations reveal that in the presence of paclitaxel the M-loop can exist in a broad range of conformations, which are in a crosstalk with the binding pose of paclitaxel. These conformations can vary from entirely unstructured ones to almost completely α-helical conformations in the low-affinity clusters 3 and 4–5, respectively. On the contrary, in the high-affinity clusters 1–2, as well as in the initial models derived from the experimental models of the complete microtubules, the M-loop appears in intermediately folded states with only a fraction of the loop adopting the α-helical structure. Remarkably, such partial structuring of M-loop was previously observed both in the experimental cryo-EM models of the complete microtubule bound to paclitaxel[4,35,37] featuring lateral contacts between protofilaments as well as in several X-ray structures of tubulin stabilized by statmin in complex with various taxane-site ligands[63], including dictyostatin[64] and discodermolide[65], as well as baccatin III and paclitaxel analog 2a[43] lacking such lateral contacts. Particularly, in the later two structures only the N-terminal fragment of M-loop adopted α-helical conformation, while the rest of the loop could not be resolved. Furthermore, the α-helical M-loop was also observed in the X-ray structures of tubulin with microtubule stabilizing macrolide compounds, laulimalide and peloruside A, bound at a different though adjacent to the M-loop pocket[66], what was later reasserted by the metadynamics simulations[67]. On the other hand, the possibility of complete unfolding of the M-loop was also shown in recent molecular dynamics simulations of taxane-bound tubulin oligomers[43]. Therefore, both the presence of taxane drugs and the lateral contacts between the adjacent protofilaments can potentially affect the conformation of the M-loop, although in the present study we could take into account only the first factor as the simulations were conducted for the model tetrameric tubulin protofilaments.

Combining the results presented here and the models suggested in previous studies one can propose that the observed transitions between the semi-ordered, and completely ordered/disordered conformations of the M-loop, which are linked to the specific binding poses of paclitaxel with high/low affinities to β-tubulin, can correlate with the microtubule stability by affecting the lateral contacts between neighboring protofilaments within the microtubule[35,37,40,43]. The latter mechanism was proposed as an alternative to the earlier hypothesis suggesting that paclitaxel acts on longitudinal tubulin contacts along protofilaments allosterically expanding the microtubule lattice[4]. Based on our results, we can hypothesize that only the distinct conformations of the partially structured M-loop (as observed in the high-affinity clusters 1 and 2 as well as in the experimental structures of protofilaments in the context of microtubules) allow for strong lateral contacts, which ultimately stabilize microtubules. On the other hand, in the low-affinity clusters, which are likely corresponding to the paclitaxel binding/unbinding intermediates, the M-loop undergoes a transition to either completely folded α-helical state (clusters 4–5) or, vice versa, a completely unordered state (cluster 3), both of which might disrupt the lateral contacts of the tubulin protofilaments and induce sterical incompatibilities between them leading to the overall decreased microtubule stability.

Indeed, the alignment of the representative structures belonging to identified clusters onto the microtubule structure indicates that in both cluster 3 and cluster 5 the M-loop appears in the conformations sterically clashing with the adjacent protofilament in contrast to the conformation of cluster 1 (see Figure S12). In principle, this observation is not surprising as the specific contacts between the neighboring protofilaments could be facilitated only by a limited number of M-loop conformations[40] accessible in the presence of paclitaxel (and apparently GTP as well), while all the alternative conformations of this flexible region (particularly those observed in the low affinity binding poses of paclitaxel in our simulations) are not compatible with the favorable protein-protein interactions between the adjacent protofilaments.

On the other hand, if the paclitaxel dissociation from β-tubulin occurs through the transient intermediates featuring such conformations of the M-loop, which are not fully compatible with the lateral contacts between the adjacent protofilaments in assembled microtubule, their presence might also affect the kinetics of paclitaxel dissociation (i.e., decrease k_{off}) resulting in a higher apparent affinity of paclitaxel to the "straight" protofilaments in the context of microtubule as compared to the "free" unassembled tubulin[48]. This effect can work complementary with an alternative mechanism where the M-loop of the apo form of β-tubulin occupies or partially occludes the paclitaxel pocket hindering its binding by decreasing k_{on} as proposed earlier[43] based on the molecular dynamics simulations of the apo form of tubulin.

Notably, several previous computational studies support the mechanism discussed above. Particularly, Mitra and Sept have shown that paclitaxel stabilizes the interactions between adjacent protofilaments by affecting the M-loop dynamics and its contacts to the H1-S2 loop of β-tubulin in the neighboring protofilament[49]. Basu et al. has further revealed that paclitaxel allosterically increases correlation between the regions of lateral contacts, i.e., the M-loop and the H1-S2 loop, already at the level of a single dimer and pinpointed that while in the apo state the M-loop forms a 310 or α-helix it tends to lose its secondary structure upon the paclitaxel binding[53]. The atomistic and coarse-grained simulations performed by Grafmüller et al.[68] additionally established the connection between the M-loop and the type of nucleotide bound to β-tubulin suggesting that local changes, particularly in the M-loop, can be induced both by the nucleotide state or by the lateral and longitudinal contacts in the aggregates of tubulin. The authors proposed that the GTP hydrolysis can induce an ordered-to-disordered transition of the M-loop resulting in a conformation, which is more favorable to form lateral contacts eventually stabilizing the microtubule.

The intricate nature of paclitaxel-tubulin interactions and the variety of paclitaxel binding poses and the M-loop conformations correlated with them, as observed in our MD simulations, align with recent findings documenting the heterogeneity of fluorescent taxanes' interactions with microtubules and their cooperative kinetics of binding and unbinding[69]. This heterogeneity may stem from the interplay between β-tubulin conformations, particularly those of the M-loop, within the microtubule lattice and the mode of paclitaxel binding and unbinding.

Analysis of key interacting residues and paclitaxel-resistant mutations

The decomposition of MM/GBSA binding energies based on the conducted simulations highlights key stabilizing and destabilizing interactions between paclitaxel and β-tubulin residues in each identified cluster. Notably, residues contributing significantly to paclitaxel affinity vary across clusters in agreement with the observed translocation of paclitaxel from the region lined by C-terminus of H7 together with the B9-B10 loop in the high-affinity conformations towards the entrance of the binding pocket surrounded by H6/H7 helices and the N-terminal region of M-loop in the low-affinity conformations. Many of these residues, which form crucial stabilizing interactions with paclitaxel, are also known in literature as being able to induce paclitaxel resistance when mutated (reviewed, for instance, in[70]). We have summarized the key residues contributing to paclitaxel binding revealed in the present study and in earlier simulations[43,51,56] in Supplementary Table S8 along with the information about the paclitaxel resistance mutations retrieved from literature. For example, the sequence analysis of resistant ovarian cancer cells from done in[71] identified point F270V and A364T (A364 of M40 isoform corresponds to S364 in βI tubulin investigated in the present study) mutations as important modulators of paclitaxel binding. Along with another resistance-inducing mutation A231T[72], all these three residues form the subpocket accommodating the phenyl group of the N-benzoyl-β-phenylisoserine side chain highlighting the importance of this moiety for paclitaxel binding[73]. Importantly, in the high-affinity conformations observed in cluster 1, this phenyl group penetrates even deeper (about 3 Å) into this subpocket (see Figure S13) suggesting that the interaction between the phenyl group and the cleft formed by B9, B10, and C-term of H7 acts as the key stabilizing hotspot. The rearrangement of the B9-B10 loop as a prerequisite for accommodation of the N-benzoyl-β-phenylisoserine side chain of a paclitaxel analog has been also noticed in[43]. In line with these observations, the replacement of the aspartic acid D26 in the vicinity of this site to the larger glutamic acid also induces the paclitaxel resistance[74] apparently due to stronger repulsion with the aromatic rings of the N-benzoyl-β-phenylisoserine chain.

In agreement with the mutations observed in the paclitaxel-resistant cancer cells mentioned earlier, the mutational analysis of taxane-resistant *S. cerevisiae* tubulin has shown that replacements of just five amino acids in β-tubulin can invoke paclitaxel sensitivity in yeast[75]. Among these substitutions, G26D and Y270F, discussed above, have been also successfully identified. Additionally, T23V and N227H are two other residues located near the N-benzoyl-β-phenylisoserine side chain of paclitaxel and strongly implicated in paclitaxel binding. In our simulations, both of them significantly contribute to the paclitaxel binding energy. Specifically, V23 is predominantly involved in the ligand binding in the high-affinity clusters, forming a hydrophobic interaction with the N-benzoyl ring, while H227 forms a stable hydrogen bond with the carbonyl oxygen of β-phenylisoserine (see Figs. 1E and 3).

Another group of residues with a high impact into the binding affinity and observed resistance mutations form the hydrophobic binding subpocket for the benzoyloxy substituent of the tetracyclic baccatin core: L215I, L217R, and L228F/R[76].

Several mutations inducing paclitaxel resistance occur in the M-loop, which is not surprising given the role of this region for the lateral microtubule interactions, which are important for the proper assembly and stability of microtubules as discussed above. A known mutation of T274 to more hydrophobic isoleucine[29] apparently results in a local rearrangement of the M-loop leading to the loss of an important H-bond between the T274 backbone and the oxetane ring of the baccatin core (Figs. 1E and 3). On the other hand, residue R282, also part of the M-loop and associated with paclitaxel resistance upon mutation to asparagine[29], neither directly contacts paclitaxel nor contributes significantly to the binding energy. However, this residue appears to stabilize the M-loop via a salt bridge to E288 (see Figure S14), which remains highly stable throughout the entire time of our MD simulations. Furthermore, another position with mutations associated with resistance, Q292H/E[72,77], is also in close proximity with E288 and the replacement of glutamine at this position to the charged amino acids may affect the stability of the salt bridge between E288 and R282.

Peculiarities of the high-affinity pose of Paclitaxel

Finally, our simulations elucidate the significance of a subpocket formed by helices H1, H7, and loop B9-B10 within the paclitaxel binding site. Cluster 1, characterized by the lowest binding energy, demonstrates an expanded paclitaxel binding pocket, facilitating enhanced penetration of the ligand into this subpocket (Fig. 4, S13). This conformational change is correlated with a *eclipsed/staggered* isomerization around a bond connecting the tetracyclic baccain core to the N-benzoyl-β-phenylisoserine side chain of paclitaxel. Interestingly, while the *staggered*-conformation is energetically unfavorable in water, the protein environment renders it equally favorable, with multiple interconversions between *eclipsed*- and *staggered*-conformations observed throughout simulations. Interactions between paclitaxel and several residues such as F270, L215, H227, and T274 significantly contribute to the lower binding energy observed in cluster 1 compared to experimental structures/cluster 2, highlighting their crucial roles in modulating paclitaxel affinity, which is also underscored by the known paxlitaxel-resistant mutations of these residues discussed above. This finding suggests a novel mode of paclitaxel binding with high affinity to β-tubulin previously unknown from experimental structures. The significant role of the observed *staggered*-conformation in this high-affinity pose suggests potential avenues for the development of modern and safer drugs. For instance, one strategy could involve replacing this moiety with an amide bond to stabilize its *staggered*-conformation.

Conclusion

Our study reveals the dynamic binding modes of paclitaxel within its binding pocket in tetrameric tubulin protofilaments through extensive atomistic molecular dynamics simulations. Paclitaxel exhibits a range of binding poses associated with neighboring residue conformational rearrangements, identified through clustering analysis. These clusters display diverse interaction patterns, correlated with MM/GBSA binding energies.

Our findings highlight the complex interplay between paclitaxel-tubulin interactions and the conformational dynamics of the M-loop, offering insights into microtubule stability. Key residues involved in paclitaxel affinity and resistance mutations are identified, providing further understanding of the ligand-binding mechanism and intermediates. Lastly, the observed *eclipsed/staggered* isomerization of a bond linking the paclitaxel core with the N-benzoyl-β-phenylisoserine side chain results in a novel high-affinity binding mode, suggesting potential directions for drug development. This study advances our knowledge of the paclitaxel mode of action and its implications for drug design strategies.

Materials and methods

Parametrization of Paclitaxel

The initial model of paclitaxel was taken from the PDB entry 3j6g[4]. Preliminary geometry optimization was carried out at the density functional theory (DFT) level using PBE0 functional and the 6–31 + G** basis set. Final geometry optimization was performed by the MP2/6-311 + G** method. Quantum mechanical calculations were performed using the software package Firefly, version 8[78]. Atomic partial charges were calculated using the RESP algorithm[79]. Molecular dynamics topology of the paclitaxel molecule was created using CGenFF service[80].

System setup

The molecular dynamics models of tubulin tetramers in complex with paclitaxel were constructed based on three distinct experimental cryoEM microtubule structures with the resolution from 5.50 to 3.50 Å: 3j6g[4], 5syf[35], and 6ew0[37] which represent all the structures of the paclitaxel-bound tubulin from a single species (*Sus scrofa*) available to date. Using the Modeller tool[81], we added unresolved amino acids in each model. The degree of protonation of ionizable amino acid residues including histidines was determined using Propka software[82], and protein cavities were located and filled with solvent molecules using the Dowser software[83]. Disulfide bridges were assigned as suggested by the pdb2gmx tool of the Gromacs suite. Each tubulin tetramer was placed in a virtual three-dimensional cubic reaction volume filled with TIP3P water. K^+ and Cl^- ions were added to the solution so that ionic strength was 0.10 M and the net charge of the system was zero. Molecular dynamics models were created using the CHARMM27 force field[84,85]. Force field parameters for GDP/GTP molecules taken from the standard CHARMM 27 library while their phosphate groups were parameterized similar to the phosphate groups of ADP/ATP[86].

Molecular dynamics simulations

We used the steepest descent algorithm to minimize the system energy. After energy minimization, a two-step equilibration occurred. On the first step we ran simulations with restrained protein heavy atoms during 1 ns, on the second – with restrained protein backbone atoms during 5 ns at constant temperature (Berendsen thermostat, 300 K, time constant 0.1 ps) and pressure (Berendsen barostat, time constant 40 ps, compressibility 4.5×10^{-5} bar $^{-1}$).

For each system, we performed three independent production runs in NPT ensemble using V-rescale thermostat (300 K, time constant 0.1 ps) and Parrinello-Rahman barostat (time constant 2 ps, compressibility 4.5×10^{-5} bar $^{-1}$)[87], each lasting at least 1 μs. To enable molecular dynamics simulations with 4 fs integration time step we applied all-bond P-LINCS constraints and mass rescaling (the partial transfer of mass from heavy atoms to bonded hydrogens)[88]. In production runs, all atoms were unrestrained. For 5syf tetramer, we performed two extra molecular dynamics simulations, wherein positional restraints were applied to the distal protein regions relative to the paclitaxel site. In particular, position restraints were applied to Cα atoms in the secondary structure elements, excluding the atoms located closer than 2 nm from the paclitaxel molecules. Molecular dynamics simulations were carried out using the GROMACS 2022.4 package[89]. VMD[90] and Pymol 2.4.2[91] were used for visualization.

All simulated systems are listed in Table S9.

Calculations of the free energy profiles

The visual inspection of paclitaxel-tubulin conformations with the lowest binding energy observed in the present simulations, pointed to the alternative conformation of the dihedral angle between the tetracyclic baccatin core to the N-benzoyl-β-phenylisoserine side chain of paclitaxel (formed by atoms OBB1, CBB, CB1, and OB1 of paclitaxel) as a potential structural prerequisite of these high-affinity paclitaxel poses. The umbrella sampling (US) approach was used to reconstruct the free energy profile for the rotation around this dihedral for free paclitaxel in water in order to further compare it with the free energy profile for the same dihedral estimated for paclitaxel bound to tubulin. The simulation system consisted of a single paclitaxel molecule obtained from the experimental structure with the PDB code 3j6g. The ligand was centered in a water box with the dimensions $5.4 \times 5.3 \times 5.2$ nm containing 4727 water molecules apart from the ligand, and 13/13 Na^+/Cl^- (corresponding to the ionic strength of 0.10 M). Firstly, a steered MD simulation (total length 50 ns, pulling rate 7.2°/ns) was carried out to generate the initial conformations for the umbrella sampling simulations with the explored dihedral taking values from − 180° to 170° with the 10° step. Then, a restrained simulation (k = 700 kJ/mol/rad.) was run for each window for 5 ns with the current value of the dihedral output each 0.1 ps. We further used gmx WHAM[92] to estimate the free energy profile from the statistics collected from individual US windows (Figure S15). The same force field and molecular dynamics parameters were used for the US simulations as for the equilibrium simulations of paclitaxel-tubulin complexes.

In order to estimate the free energy profile for the same dihedral from the protofilament simulations, we have employed the Boltzmann inversion to the corresponding probability density of the dihedral values:

$$\Delta G = -RTln(P),$$

where R is the gas constant, T - temperature, P - the probability density.

Analysis

We analyzed the conformations of paclitaxel in its binding site by consequently applying principal component analysis and agglomerative clustering to the cartesian coordinates of heavy atoms belonging to the ligand and to the amino acid residues forming the binding pocket upon their roto-translational alignment to the initial experimental structure with the PDB code 3j6g. Since each simulated tubulin tetramer comprised two paclitaxel binding sites, both of them were processed separately, thereby effectively doubling the number of sampled conformations. Residues were deemed part of the binding site if, at least in one of the initial experimental structures or the simulation frames, the distance between paclitaxel and at least one heavy atom of a residue did not exceed 7 Å. The selection of the distance cut-off was guided by the thresholds used for various intermolecular interactions in the Protein–Ligand Interaction Profiler (PLIP)[93]. It resulted in a shortlist comprising 86 residues, detailed in Table S10. Principal component analysis (PCA) was applied to the aligned atomic positions of paclitaxel and the binding site residues to reduce the dimensionality of the original trajectories and facilitate further clustering. Given that the conformational transitions observed in the simulations are mainly associated with large-scale paclitaxel movements and M-loop rearrangements, which are in the focus of the present study, we believe that the employed cartesian PCA could successfully catch relevant motions. However, more sophisticated approaches for the selection of collective variables reported earlier, e.g[94–96]. , might be beneficial for in depth analysis in future. The agglomerative clustering was performed employing the scikit-learn library with the average linkage over the top 2 principal components, which explained 57% of the dataset variance (Figure S16). The low cosine content of the top principal components (0.113, 0.097, and 0.042 for PC1, PC2, and PC3, respectively) imply that sufficient sampling of the conformational ensemble was achieved[97]. The determination of the optimal number of clusters was accomplished through the silhouette metrics (Figure S17).

We further estimated the paclitaxel binding free energies for the all of obtained molecular dynamics trajectories as well as for the initial experimental structures using the Molecular Mechanics Generalized Born Surface Area (MM/GBSA) approach as realized in gmx_MMPBSA[98], which also allowed us to decompose the ΔG_{bind} into contributions of individual amino acids. The default protocol for protein-ligand complexes was used.

MDAnalysis 2.4.2 [99] was used for PCA, calculation of root mean square displacement (RMSD) and fluctuations (RMSF), other manipulations with coordinates, while mdtraj 1.9.7 [100] was used for the secondary structure assignment.

The matrix of transitions between the identified clusters was calculated for the joint trajectory (19100 frames in total) and visualized using pyEMMA[101].

Data availability

All the trajectories, starting conformations, representative conformations of identified clusters, topologies, and Gromacs mdp parameters are available on Zenodo (https://zenodo.org/records/12513444*)*. Molecular dynamics simulations were carried out using the GROMACS 2022.4 package (https://manual.gromacs.org/*)*. gmx_MMPBSA (https://valdes-tresanco-ms.github.io/gmx_MMPBSA*)*, MDAnalysis 2.4.2 (https://www.mdanalysis.org/*)*, and mdtraj 1.9.7 (https://www.mdtraj.org/1.9.7/index.html*)* were used for the trajectory analysis. Firefly (http://classic.chem.msu.su/gran/gamess/index.html*)* and CgenFF (https://cgenff.silcsbio.com/*)* were used to develop the ligand topology. Pymol 2.4.2 (https://www.pymol.org/*)*, pyEMMA 2 (http://www.emma-project.org/latest/*)* and VMD 1.9.4 (https://www.ks.uiuc.edu/Research/vmd/) were used for visualization.

Received: 30 November 2024; Accepted: 3 March 2025
Published online: 11 March 2025

References

1. Rowinsky, E. K. & Donehower, R. C. Paclitaxel (taxol). *N Engl. J. Med.* **332**, 1004–1014 (1995).
2. Nogales, E., Wolf, S. G. & Downing, K. H. Structure of the αβ tubulin dimer by electron crystallography. *Nature* 391, 199–203. https://doi.org/10.1038/34465 (1998).
3. Nogales, E., Whittaker, M., Milligan, R. A. & Downing, K. H. High-Resolution Model of the Microtubule. *Cell* 96, 79–88. https://doi.org/10.1016/s0092-8674(00)80961-7 (1999).
4. Alushin, G. M. et al. High-resolution microtubule structures reveal the structural transitions in αβ-tubulin upon GTP hydrolysis. *Cell* **157**, 1117–1129 (2014).
5. Chrétien, D., Metoz, F., Verde, F., Karsenti, E. & Wade, R. H. Lattice defects in microtubules: protofilament numbers vary within individual microtubules. *J. Cell Biol.* 117, 1031–1040. https://doi.org/10.1083/jcb.117.5.1031 (1992).
6. Wade, R. H., Chrétien, D. & Job, D. Characterization of microtubule protofilament numbers. *Journal of Molecular Biology* 212, 775–786. https://doi.org/10.1016/0022-2836(90)90236-f (1990).
7. Brouhard, G. J. & Rice, L. M. The contribution of αβ-tubulin curvature to microtubule dynamics. *J. Cell. Biol.* **207**, 323–334 (2014).
8. Nogales, E., Wang, H. W. & Niederstrasser, H. Tubulin rings: which way do they curve? *Curr. Opin. Struct. Biol.* **13**, 256–261 (2003).
9. Nogales, E. & Wang, H. W. Structural mechanisms underlying nucleotide-dependent self-assembly of tubulin and its relatives. *Curr. Opin. Struct. Biol.* **16**, 221–229 (2006).
10. Fedorov, V. A. et al. Mechanical properties of tubulin intra- and inter-dimer interfaces and their implications for microtubule dynamic instability. *PLoS Comput. Biol.* **15**, e1007327 (2019).
11. Mitchison, T. & Kirschner, M. Dynamic instability of microtubule growth. *Nature* **312**, 237–242 (1984).
12. Gebremichael, Y., Chu, J. W. & Voth, G. A. Intrinsic bending and structural rearrangement of tubulin dimer: molecular dynamics simulations and coarse-grained analysis. *Biophys. J.* **95**, 2487–2499 (2008).
13. Löwe, J., Li, H., Downing, K. H. & Nogales, E. Refined structure of alpha beta-tubulin at 3.5 A resolution. *J. Mol. Biol.* **313**, 1045–1057 (2001).

14. Snyder, J. P., Nettles, J. H., Cornett, B., Downing, K. H. & Nogales, E. The binding conformation of taxol in beta-tubulin: a model based on electron crystallographic density. *Proc. Natl. Acad. Sci. U. S. A.* **98**, 5312–5316 (2001).
15. Geney, R. et al. Use of the tubulin bound Paclitaxel conformation for structure-based rational drug design. *Chem. Biol.* **12**, 339–348 (2005).
16. Paik, Y. ⊥. et al. Rotational-Echo Double-Resonance NMR distance measurements for the Tubulin-Bound Paclitaxel conformation. https://doi.org/10.1021/ja0656604 (2006).
17. Li, Y. ‡. et al. Conformation of Microtubule-Bound Paclitaxel determined by fluorescence spectroscopy and REDOR NMR†. https://doi.org/10.1021/bi991936r (1999).
18. Conformation of Taxotere®. and analogues determined by NMR spectroscopy and molecular modeling studies. *CoLab*. https://colab.ws/articles/10.1016%2FS0040-4020%2801%2981822-6.
19. Snyder*†, J. P., Nevins, N., Cicero, D. O. & Jansen§ ‡. And J. The Conformations of Taxol in Chloroform. https://doi.org/10.1021/ja9930115 (2000).
20. Vander Velde, D. G., Georg, G. I., Grunewald, G. L., Gunn, C. W. & Mitscher, L. A. 'Hydrophobic collapse' of taxol and taxotere solution conformations in mixtures of water and organic solvent. https://doi.org/10.1021/ja00077a095 (2002).
21. Ojima, I. et al. A common pharmacophore for cytotoxic natural products that stabilize microtubules. *Proc. Natl. Acad. Sci. U. S. A.* **96**, 4256–4261 (1999).
22. Ojima*†, I. et al. A Novel Approach to the Study of Solution Structures and Dynamic Behavior of Paclitaxel and Docetaxel Using Fluorine-Containing Analogs as Probes. https://doi.org/10.1021/ja9633777 (1997).
23. Ojima, I. *. et al. Macrocycle formation by Ring-Closing metathesis. Application to the syntheses of novel macrocyclic taxoids. https://doi.org/10.1021/ja000293w (2000).
24. Geng, X., Miller, M. L., Lin, S. & Ojima, I. Synthesis of novel C2-C3'N-linked macrocyclic taxoids by means of highly regioselective heck macrocyclization. *Org. Lett.* **5**, 3733–3736 (2003).
25. Metaferia, B. B. et al. Synthesis and biological evaluation of novel macrocyclic Paclitaxel analogues. *Org. Lett.* **3**, 2461–2464 (2001).
26. Boge, T. C., Wu, Z. J., Himes, R. H., Velde, V., Georg, G. & D. G. & I. Conformationally restricted Paclitaxel analogues: macrocyclic mimics of the 'hydrophobic collapse' conformation. *Bioorg. Med. Chem. Lett.* **9**, 3047–3052 (1999).
27. Querolle, O. et al. Synthesis of novel macrocyclic docetaxel analogues. Influence of their macrocyclic ring size on tubulin activity. *J. Med. Chem.* **46**, 3623–3630 (2003).
28. Ganesh, T. et al. The bioactive taxol conformation on beta-tubulin: experimental evidence from highly active constrained analogs. *Proc. Natl. Acad. Sci. U. S. A.* **101**, 10006–10011 (2004).
29. Giannakakou, P. et al. A common pharmacophore for epothilone and taxanes: molecular basis for drug resistance conferred by tubulin mutations in human cancer cells. *Proc. Natl. Acad. Sci. U. S. A.* **97**, 2904–2909 (2000).
30. He, L. et al. A common pharmacophore for taxol and the epothilones based on the biological activity of a taxane molecule lacking a C-13 side chain. *Biochemistry* **39**, 3972–3978 (2000).
31. Alcaraz, A. A., Mehta, A. K., Johnson, S. A. & Snyder, J. P. The T-Taxol conformation. *J. Med. Chem.* **49**, 2478–2488 (2006).
32. Yang, Y., Alcaraz, A. A. & Snyder, J. P. The tubulin-bound conformation of Paclitaxel: T-taxol vs 'PTX-NY'. *J. Nat. Prod.* **72**, 422–429 (2009).
33. Baker, J. K. Nuclear overhauser effect spectroscopy (NOESY) and dihedral angle measurements in the determination of the conformation of taxol in solution. *Spectrosc. Lett.* https://doi.org/10.1080/00387019208020754 (1992).
34. NMR and molecular modeling study of the conformations of taxol and of its side chain methylester in aqueous and non-aqueous solution. *Tetrahedron* **49**, 6545–6560 (1993).
35. Kellogg, E. H. et al. Insights into the distinct mechanisms of action of taxane and Non-Taxane microtubule stabilizers from Cryo-EM structures. *J. Mol. Biol.* **429**, 633–646 (2017).
36. DebsG. E., Cha, M., Liu, X., Huehn, A. R. & Sindelar, C. V. Dynamic and asymmetric fluctuations in the microtubule wall captured by high-resolution cryoelectron microscopy. *Proc. Natl. Acad. Sci. U. S. A.* **117**, 16976–16984 (2020).
37. Manka, S. W. & Moores, C. A. The role of tubulin-tubulin lattice contacts in the mechanism of microtubule dynamic instability. *Nat. Struct. Mol. Biol.* **25**, 607–615 (2018).
38. Howes, S. C. et al. Structural differences between yeast and mammalian microtubules revealed by cryo-EM. *J. Cell. Biol.* **216**, 2669–2677 (2017).
39. Arellano-Santoyo, H. et al. Multimodal tubulin binding by the yeast kinesin-8, Kip3, underlies its motility and depolymerization. *bioRxiv* 2021.10.12.464151. https://doi.org/10.1101/2021.10.12.464151 (2021).
40. Debs, G. E., Cha, M., Liu, X., Huehn, A. R. & Sindelar, C. V. Dynamic and asymmetric fluctuations in the microtubule wall captured by high-resolution cryoelectron microscopy. *Proc. Natl. Acad. Sci. U. S. A.* 117, 16976–16984 (2020).
41. Elie-Caille, C. et al. Straight GDP-Tubulin Protofilaments Form in the Presence of Taxol. *Current Biology* 17, 1765–1770. https://doi.org/10.1016/j.cub.2007.08.063 (2007).
42. Amos, L. A. & Löwe, J. How taxol stabilises microtubule structure. *Chem. Biol.* **6**, R65–R69 (1999).
43. Prota, A. E. et al. Structural insight into the stabilization of microtubules by taxanes. *Elife* 12, (2023).
44. Buey, R. M. et al. Interaction of epothilone analogs with the Paclitaxel binding site: relationship between binding affinity, microtubule stabilization, and cytotoxicity. *Chem. Biol.* **11**, 225–236 (2004).
45. Schiff, P. B. & Horwitz, S. B. Taxol assembles tubulin in the absence of exogenous Guanosine 5'-triphosphate or microtubule-associated proteins. *Biochemistry* **20**, 3247–3252 (1981).
46. Carlier, M. F. & Pantaloni, D. Taxol effect on tubulin polymerization and associated Guanosine 5'-triphosphate hydrolysis. *Biochemistry* **22**, 4814–4822 (1983).
47. Howard, W. D. & Timasheff, S. N. Linkages between the effects of Taxol, Colchicine, and GTP on tubulin polymerization. *J. Biol. Chem.* **263**, 1342–1346 (1988).
48. Díaz, J. F., Menéndez, M. & Andreu, J. M. Thermodynamics of ligand-induced assembly of tubulin. *Biochemistry* **32**, 10067–10077 (1993).
49. Mitra, A. & Sept, D. Taxol allosterically alters the dynamics of the tubulin dimer and increases the flexibility of microtubules. *Biophys. J.* **95**, 3252–3258 (2008).
50. Natarajan, K. & Senapati, S. Understanding the basis of drug resistance of the mutants of αβ-tubulin dimer via molecular dynamics simulations. *PLoS One* **7**, e42351 (2012).
51. Churchill, C. D. M., Klobukowski, M. & Tuszynski, J. A. Elucidating the mechanism of action of the clinically approved taxanes: a comprehensive comparison of local and allosteric effects. *Chem. Biol. Drug Des.* **86**, 1253–1266 (2015).
52. Tripathi, S., Srivastava, G. & Sharma, A. Molecular dynamics simulation and free energy landscape methods in probing L215H, L217R and L225M βI-tubulin mutations causing Paclitaxel resistance in cancer cells. *Biochem. Biophys. Res. Commun.* **476**, 273–279 (2016).
53. Basu, D., Majumdar, S., Mandal, N. & Dastidar, S. G. Mechanisms of influence of the microtubule over-stabilizing ligands on the structure and intrinsic dynamics of α,β-Tubulin. *Comput. Biol. Chem.* **96**, 107617 (2022).
54. Karthikeyan, S. et al. Exploring the binding interaction mechanism of taxol in β-Tubulin and bovine serum albumin: A biophysical approach. *Mol. Pharm.* https://doi.org/10.1021/acs.molpharmaceut.8b00948 (2019).
55. Ghadari, R., Alavi, F. S. & Zahedi, M. Evaluation of the effect of the chiral centers of taxol on binding to β-tubulin: A Docking and molecular dynamics simulation study. *Comput. Biol. Chem.* **56**, 33–40 (2015).

56. Xu, S. et al. Molecular dynamics simulation and density functional theory studies on the active pocket for the binding of Paclitaxel to tubulin. *J. Mol. Model.* **18**, 377–391 (2012).
57. Fedorov, V. A., Kholina, E. G. & Kovalenko, I. B. Molecular dynamics of tubulin protofilaments and the effect of taxol on their bending deformation. *Comput. Res. Model.* **16**, 503–512 (2024).
58. Díaz, J. F., Barasoain, I. & Andreu, J. M. Fast kinetics of taxol binding to microtubules. Effects of solution variables and microtubule-associated proteins. *J. Biol. Chem.* **278**, 8407–8419 (2003).
59. Peng, L. X., Hsu, M. T., Bonomi, M., Agard, D. A. & Jacobson, M. P. The free energy profile of tubulin straight-bent conformational changes, with implications for microtubule assembly and drug discovery. *PLoS Comput. Biol.* **10**, e1003464 (2014).
60. Igaev, M. & Grubmüller, H. Microtubule assembly governed by tubulin allosteric gain in flexibility and lattice induced fit. *Elife* **7**, (2018).
61. Natarajan, K., Mohan, J. & Senapati, S. Relating nucleotide-dependent conformational changes in free tubulin dimers to tubulin assembly. *Biopolymers* **99**, 282–291 (2013).
62. Grafmüller, A. & Voth, G. A. Intrinsic bending of microtubule protofilaments. *Structure* **19**, 409–417 (2011).
63. Prota, A. E. et al. Molecular mechanism of action of microtubule-stabilizing anticancer agents. *Science* **339**, 587–590 (2013).
64. Trigili, C. et al. Structural determinants of the Dictyostatin chemotype for tubulin binding affinity and antitumor activity against Taxane- and Epothilone-Resistant Cancer cells. *ACS Omega* **1**, 1192–1204 (2016).
65. Prota, A. E. et al. Structural basis of microtubule stabilization by discodermolide. *Chembiochem* **18**, 905–909 (2017).
66. Prota, A. E. et al. Structural basis of microtubule stabilization by Laulimalide and Peloruside A. *Angew Chem. Int. Ed. Engl.* **53**, 1621–1625 (2014).
67. Castro-Alvarez, A., Pineda, O. & Vilarrasa, J. Further insight into the interactions of the cytotoxic macrolides Laulimalide and Peloruside A with their common binding site. *ACS Omega*. **3**, 1770–1782 (2018).
68. Grafmüller, A., Noya, E. G. & Voth, G. A. Nucleotide-dependent lateral and longitudinal interactions in microtubules. *J. Mol. Biol.* **425**, 2232–2246 (2013).
69. Rai, A. et al. Taxanes convert regions of perturbed microtubule growth into rescue sites. *Nat. Mater.* **19**, 355–365 (2020).
70. Huzil, J. T., Chen, K., Kurgan, L. & Tuszynski, J. A. The roles of β-tubulin mutations and isotype expression in acquired drug resistance. *Cancer Inf.* **3**, 117693510700300 (2007).
71. Giannakakou, P. et al. Paclitaxel-resistant human ovarian cancer cells have mutant beta-tubulins that exhibit impaired paclitaxel-driven polymerization. *J. Biol. Chem.* **272**, 17118–17125 (1997).
72. Verrills, N. M. et al. Microtubule alterations and mutations induced by Desoxyepothilone B: implications for drug-target interactions. *Chem. Biol.* **10**, 597–607 (2003).
73. Kingston, D. G. Taxol: the chemistry and structure-activity relationships of a novel anticancer agent. *Trends Biotechnol.* **12**, 222–227 (1994).
74. Hari, M. et al. Paclitaxel-resistant cells have a mutation in the paclitaxel-binding region of beta-tubulin (Asp26Glu) and less stable microtubules. *Mol. Cancer Ther.* **5**, 270–278 (2006).
75. Dostál, V. & Libusová, L. Microtubule drugs: action, selectivity, and resistance across the kingdoms of life. *Protoplasma* **251**, 991–1005 (2014).
76. Gonzalez-Garay, M. L., Chang, L., Blade, K., Menick, D. R. & Cabral, F. A beta-tubulin leucine cluster involved in microtubule assembly and Paclitaxel resistance. *J. Biol. Chem.* **274**, 23875–23882 (1999).
77. Wang, Y., Veeraraghavan, S. & Cabral, F. Intra-allelic suppression of a mutation that stabilizes microtubules and confers resistance to colcemid. *Biochemistry* **43**, 8965–8973 (2004).
78. Granovsky, A. A. www Firefly version 7.1. G. http://classic.chem.msu.su/gran/gamess/index. *html* (2012).
79. Bayly, C. I., Cieplak, P., Cornell, W. & Kollman, P. A. A well-behaved electrostatic potential based method using charge restraints for deriving atomic charges: the RESP model. *J. Phys. Chem.* **97**, 10269–10280 (1993).
80. Vanommeslaeghe, K. & MacKerell, A. D. Jr. Automation of the CHARMM general force field (CGenFF) I: bond perception and atom typing. *J. Chem. Inf. Model.* **52**, 3144–3154 (2012).
81. Webb, B. & Sali, A. Comparative protein structure modeling using MODELLER. *Curr. Protoc. Bioinf.* **47**, 561–532 (2014).
82. Olsson, M. H. M., Søndergaard, C. R., Rostkowski, M. & Jensen, J. H. PROPKA3: consistent treatment of internal and surface residues in empirical pKa predictions. *J. Chem. Theory Comput.* **7**, 525–537 (2011).
83. Morozenko, A. & Stuchebrukhov, A. A. Dowser++, a new method of hydrating protein structures. *Proteins* **84**, 1347–1357 (2016).
84. MacKerell, A. D. et al. All-atom empirical potential for molecular modeling and dynamics studies of proteins. *J. Phys. Chem. B.* **102**, 3586–3616 (1998).
85. MacKerell, A. D. Jr, Feig, M. & Brooks, C. L. Improved treatment of the protein backbone in empirical force fields. *J. Am. Chem. Soc.* **126**, 698–699 (2004). 3rd.
86. Pavelites, J. J., Gao, J., Bash, P. A. & Mackerell, A. D. A molecular mechanics force field for NAD + NADH, and the pyrophosphate groups of nucleotides. *J. Comput. Chem.* **18**, 221–239 (1997).
87. Parrinello, M. & Rahman, A. Polymorphic transitions in single crystals: A new molecular dynamics method. *J. Appl. Phys.* **52**, 7182–7190 (1981).
88. Feenstra, K. A., Hess, B. & Berendsen, H. J. C. Improving efficiency of large time-scale molecular dynamics simulations of hydrogen-rich systems. *J. Comput. Chem.* **20**, 786–798 (1999).
89. Páll, S. et al. Heterogeneous parallelization and acceleration of molecular dynamics simulations in GROMACS. *J. Chem. Phys.* **153**, 134110 (2020).
90. Humphrey, W., Dalke, A. & Schulten, K. VMD: visual molecular dynamics. *J. Mol. Graph.* **14**, 33–38 (1996).
91. DeLano, W. L. et al. Pymol: an open-source molecular graphics tool. *CCP4 Newsl. Protein Crystallogr.* **40**, 82–92 (2002).
92. Hub, J. S., de Groot, B. L. & van der Spoel, D. g_wham—A free weighted histogram analysis implementation including robust error and autocorrelation estimates. *J. Chem. Theory Comput.* **6**, 3713–3720 (2010).
93. Salentin, S., Schreiber, S., Haupt, V. J., Adasme, M. F. & Schroeder, M. PLIP: fully automated protein-ligand interaction profiler. *Nucleic Acids Res.* **43**, W443–W447 (2015).
94. Mendels, D., Piccini, G. & Parrinello, M. Collective variables from local fluctuations. *J. Phys. Chem. Lett.* **9**, 2776–2781 (2018).
95. Noé, F. & Clementi, C. Collective variables for the study of long-time kinetics from molecular trajectories: theory and methods. *Curr. Opin. Struct. Biol.* **43**, 141–147 (2017).
96. Wu, J., Xue, W. & Voth, G. A. -Means clustering Coarse-Graining (KMC-CG): A next generation methodology for determining optimal Coarse-Grained mappings of large biomolecules. *J. Chem. Theory Comput.* **19**, 8987–8997 (2023).
97. Maisuradze, G. G., Liwo, A. & Scheraga, H. A. Principal component analysis for protein folding dynamics. *J. Mol. Biol.* **385**, 312–329 (2009).
98. Valdés-Tresanco, M. S., Valdés-Tresanco, M. E., Valiente, P. A., Moreno, E. gmx_MMPBSA: A new tool to perform End-State free energy calculations with GROMACS. *J. Chem. Theory Comput.* **17**, 6281–6291 (2021).
99. Michaud-Agrawal, N., Denning, E. J., Woolf, T. B. & Beckstein, O. MDAnalysis: a toolkit for the analysis of molecular dynamics simulations. *J. Comput. Chem.* **32**, 2319–2327 (2011).
100. McGibbon, R. T. et al. MDTraj: A modern open library for the analysis of molecular dynamics trajectories. *Biophys. J.* **109**, 1528–1532 (2015).
101. Scherer, M. K. et al. PyEMMA 2: A Software Package for Estimation, Validation, and Analysis of Markov Models. https://doi.org/10.1021/acs.jctc.5b00743 (2015).

Acknowledgements
The work was supported by the Russian Science Foundation, project № 23-74-00007 to I.B.K. supporting the molecular dynamics simulations. Molecular dynamics simulations were carried out using the equipment of the shared research facilities of the high-performance computational resources at Lomonosov Moscow State University. M.E.B. and P.S.O. are part of an innovative drug development team based on structural biology and bioinformatics at Shenzhen MSU-BIT University #2022KCXTD034 supporting data analysis.

Author contributions
P.O. and N.G. designed and supervised the study. V.F. , E.K., and I.K. conducted the simulations. M.B. and P.O. performed the analyses. M.B. and P.O. wrote the manuscript with contributions from N.G. All authors reviewed the manuscript.

Declarations

Competing interests
The authors declare no competing interests.

Additional information
Supplementary Information The online version contains supplementary material available at https://doi.org/10.1038/s41598-025-92805-z.

Correspondence and requests for materials should be addressed to N.G. or P.O.

Reprints and permissions information is available at www.nature.com/reprints.

Publisher's note Springer Nature remains neutral with regard to jurisdictional claims in published maps and institutional affiliations.